Supporting Information for "A comprehensive picture for binary interactions of subaqueous barchans"

W. R. Assis[1], E. M. Franklin[2]

[1,2]School of Mechanical Engineering, UNICAMP - University of Campinas,

Rua Mendeleyev, 200, Campinas, SP, Brazil

Contents of this file

1. Figures S1 to S25

2. Tables S1 and S2

Additional Supporting Information (Files uploaded separately)

1. Captions for Movies S1 to S10

Introduction

This supporting information presents the layout of the experimental device, a photograph of the test section, microscopy images of the used grains, lists of the tested conditions, snapshots of barchan interactions with different initial conditions and grain types, additional graphics, and movies showing examples of each collision pattern. We note that

all individual images that were processed to plot Figs. 3e and 3f of the paper are available on Mendeley Data (http://dx.doi.org/10.17632/jn3kt83hzh).

The experiments described in the paper were conducted in a water channel of transparent material, for which the layout and a photograph of the test section are shown in Figs. S1 and S2, respectively. With the channel previously filled with water, controlled grains were poured inside, forming a pair of bedforms in either aligned or off-centered configurations. By imposing a water flow, each bedform was deformed into a barchan shape and interacted with each other.

A camera of complementary metal-oxide-semiconductor (CMOS) type was placed above the channel in order to acquire images of the bedforms. The camera resolution was of 1920 px $\times$ 1080 px at 60 Hz and it was mounted on a traveling system, both controlled by a computer. Depending on the tested conditions, the region of interest (ROI) was set to 1920 px $\times$ 701 px or to 1920 px $\times$ 801 px, and the frequency to 30 Hz. We used a lens of 60 mm focal distance and F2.8 maximum aperture mounted on the camera, and lamps of light-emitting diode (LED) were branched to a continuous-current source to provide the necessary light. The conversion from px to a physical system of units was made by means of a scale placed in the channel previously filled with water. The acquired images were processed by numerical scripts written in the course of this work. They basically removed the image background, binarized the images, and identified the main morphological properties of barchans and their relative distances.

Two observations are made just below concerning imperfections in our data on dune-dune interaction.

OBS1: in Fig.S23 (below), test runs 1, 2, 3, 29, 33, 34 and 37 were in the frontier between the exchange and merging patterns, the resulting quantity of ejected grains being so small that the ejected bedform spread out as soon as it was ejected. We classified these experimental points as exchange, but we understand that they could have been classified as merging as well.

OBS2: in Fig.S23 (below), the image recordings of test runs 24 and 44 were interrupted just before the end of the interaction process between barchans. This happened because the translation mechanism arrived at its end position. However, we observed that in both cases the interaction pattern was the fragmentation-chasing one (which can also be guessed from the respective movies).

Concerning the water flow, experiments with particle image velocimetry (PIV) were performed in the test section of the channel in the absence of grains, and they are described in detail in previous works cited in the paper. For the PIV experiments, a laser sheet was positioned in the vertical plane of symmetry of the channel, and a charge-coupled device (CCD) camera was placed orthogonally to that sheet. Different flow rates were then imposed in the channel without the presence of grains (mono-phase water flow). The laser was of dual-cavity Nd:YAG Q-switched type capable to emit 2×130 mJ at a maximum pulse rate of 15 Hz and the camera sensor had a size of $7.4\ \mu\text{m} \times 7.4\ \mu\text{m}$ (px^2), with a spatial resolution of 2048 px $\times$ 2048 px. When synchronized, the camera and laser were operated at 4 Hz for the acquisition of image pairs, and the time between frames was adjusted in accordance with the flow velocities. We employed hollow glass beads 10

μm in diameter with a specific gravity of 1.05 as seeding particles, and the magnification was of approximately 0.1.

We obtained profiles following closely the law of the wall, $u^+ = 1/\kappa \ln y^+ + B$, where u^+ is the mean velocity normalized by the shear velocity u_*, $\kappa = 0.41$ is the von Kármán constant, $y^+ = y\nu/u_*$ is the vertical coordinate normalized by the viscous length, ν is the kinematic viscosity and B is a constant. An example of measured profile is given in Fig. S10, which follows a hydraulic smooth regime. From the profile inclination, we found the experimental values of u_* and Darcy friction factor f. The latter was then compared with the friction factor obtained from the Blasius correlation, $f_{bla} = 0.316 Re_{dh}^{-1/4}$, where $Re_{dh} = U d_h/\nu$ is the Reynolds number based on the hydraulic diameter, U being the cross-sectional mean velocity and $d_h = 3.05\ \delta$ (d_h is the cross-sectional area multiplied by four and divided by the cross-sectional perimeter). Table S1 presents the values of U, u_*, f and f_{bla} obtained for the bottom wall of the channel for each Reynolds number. From Tab. S1, we observe that differences between the experimental and correlated friction factors are equal or less than 6 % (proportional to u_*^2, and then to the Shields number), implying differences in u_* of less than 3 %.

Movie S1. Chasing_Alig.gif Movie showing an example of the chasing pattern in aligned configuration

Movie S2. Chasing_Stag.gif Movie showing an example of the chasing pattern in off-centered configuration

Movie S3. Merging_Alig.gif Movie showing an example of the merging pattern in aligned configuration

Movie S4. Merging_Stag.gif Movie showing an example of the merging pattern in off-centered configuration

Movie S5. Exchange_Alig.gif Movie showing an example of the exchange pattern in aligned configuration

Movie S6. Exchange_Stag.gif Movie showing an example of the exchange pattern in off-centered configuration

Movie S7. Fragmentation_Chasing_Alig.gif Movie showing an example of the fragmentation-chasing pattern in aligned configuration

Movie S8. Fragmentation_Chasing_Stag.gif Movie showing an example of the fragmentation-chasing pattern in off-centered configuration

Movie S9. Fragmentation_Exchange_Alig.gif Movie showing an example of the fragmentation-exchange pattern in aligned configuration

Movie S10. Fragmentation_Exchange_Stag.gif Movie showing an example of the fragmentation-exchange pattern in off-centered configuration

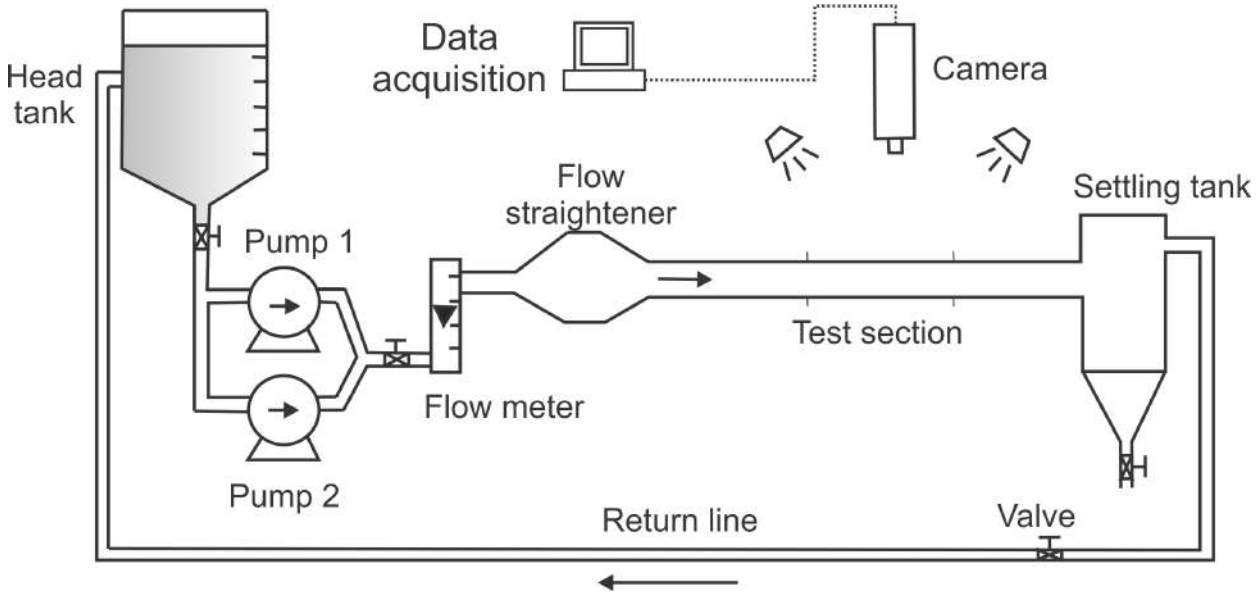

Figure S1. Layout of the experimental setup.

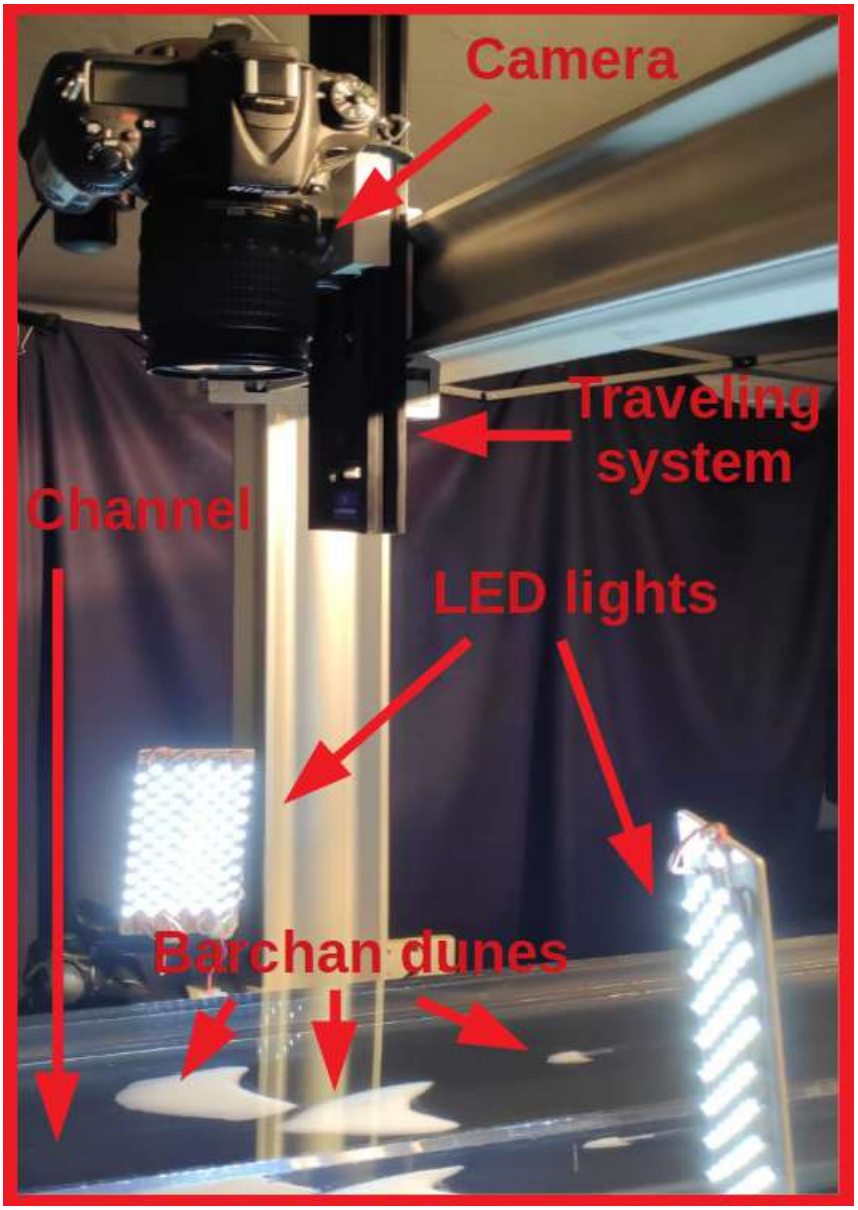

Figure S2. Photograph of the test section.

Figure S3. Microscopy image for the 0.40 mm $\leq d \leq$ 0.60 mm round glass beads of white color.

Figure S4. Microscopy image for the 0.40 mm $\leq d \leq$ 0.60 mm round glass beads of red color.

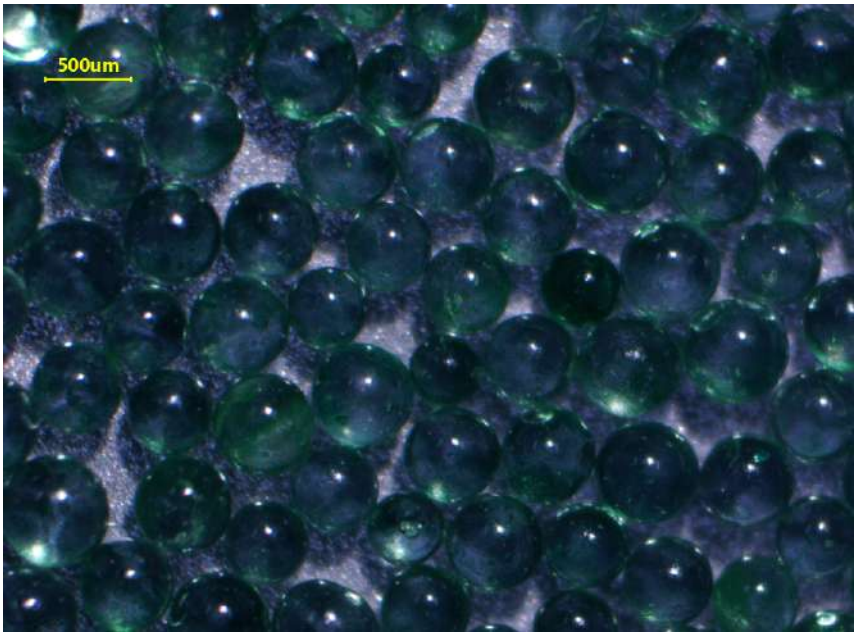

Figure S5. Microscopy image for the 0.40 mm $\leq d \leq$ 0.60 mm round glass beads of green color.

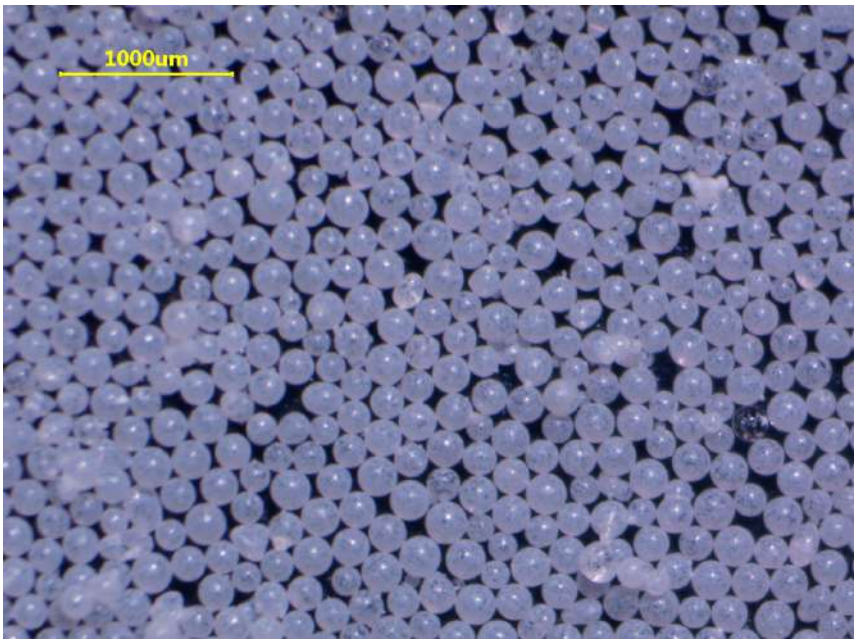

Figure S6. Microscopy image for the 0.15 mm $\leq d \leq$ 0.25 mm round glass beads of white color.

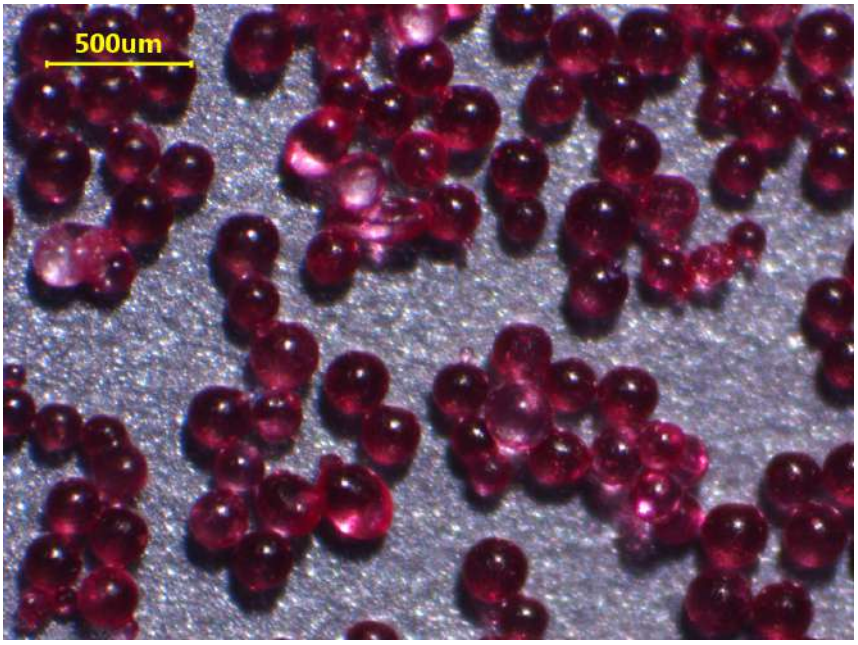

Figure S7. Microscopy image for the 0.15 mm $\leq d \leq$ 0.25 mm round glass beads of red color.

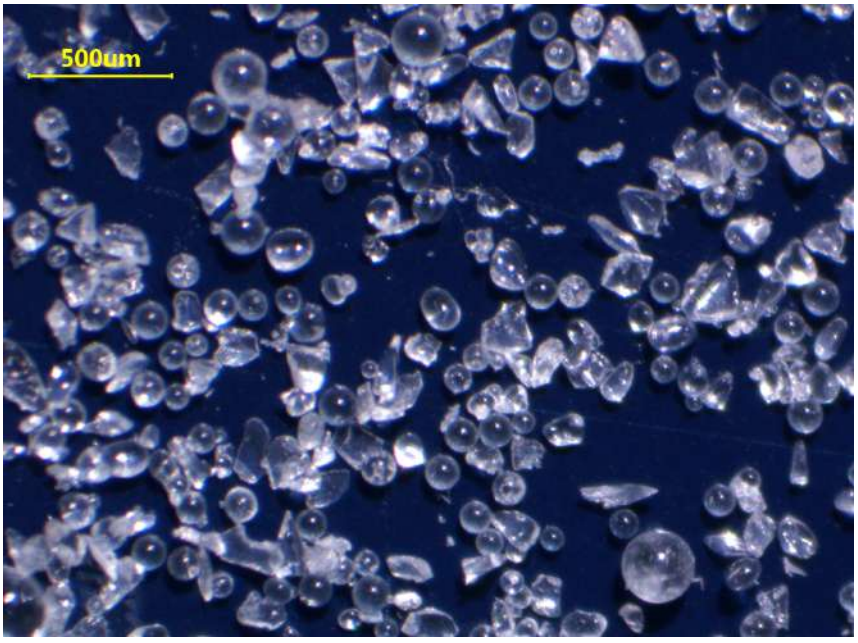

Figure S8. Microscopy image for the 0.21 mm $\leq d \leq$ 0.30 mm angular glass beads.

Figure S9. Microscopy image for the 0.40 mm $\leq d \leq$ 0.60 mm round zirconium beads.

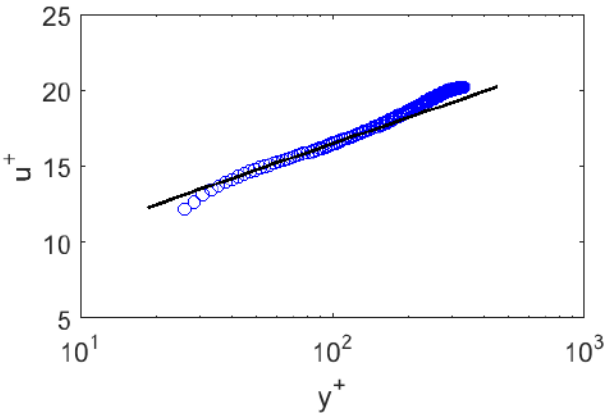

Figure S10. Velocity profile over the bottom wall of the channel in log-normal scales. Circles correspond to experimental points and the continuous line to the inclination of the logarithmic region.

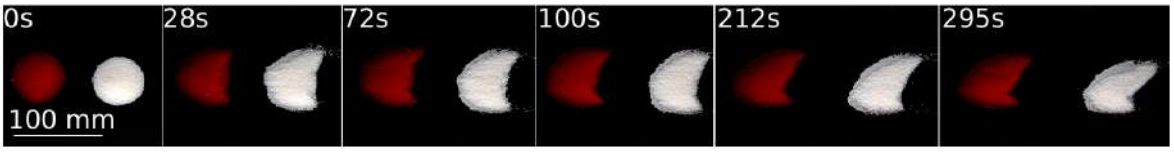

(a)

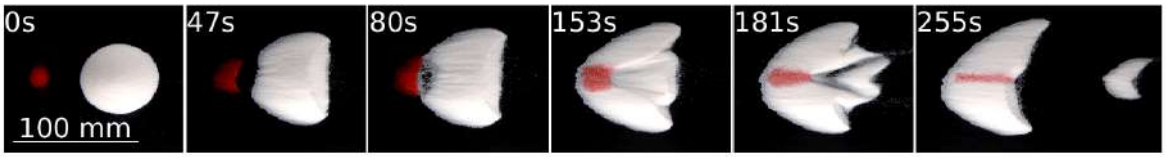

(b)

Figure S11. Snapshots of barchan interactions for aligned dunes, with two conical piles as initial condition. In the snapshots, the water flow is from left to right, the upstream pile consisting of red (darker) glass beads and the downstream pile of white (clearer) glass beads. In Fig. (a), 0.40 mm $\leq d \leq$ 0.60 mm, in Fig. (b) 0.15 mm $\leq d \leq$ 0.25 mm, and the corresponding times are shown in each frame. (a) Chasing, equivalent to test 61 of Fig. S23, but with two initial conical piles; (b) exchange, equivalent to test 36 of Fig. S23, but with two initial conical piles.

(a)

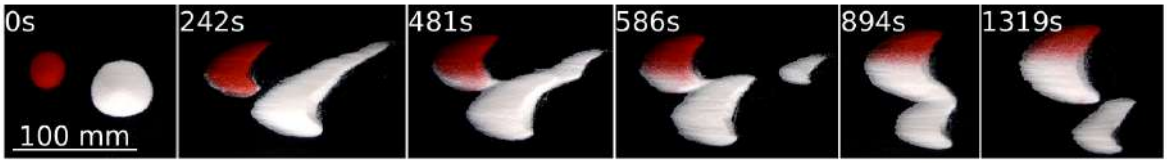

(b)

Figure S12. Snapshots of barchan interactions for off-centered dunes, with two conical piles as initial condition. In the snapshots, the water flow is from left to right, the upstream pile consisting of red (darker) glass beads and the downstream pile of white (clearer) glass beads. In Fig. (a), 0.40 mm $\leq d \leq$ 0.60 mm, in Fig. (b) 0.15 mm $\leq d \leq$ 0.25 mm, and the corresponding times are shown in each frame. (a) Merging (test 14 of Fig. S24); (b) fragmentation-exchange, equivalent to test 5 of Fig. S24, but with two initial conical piles.

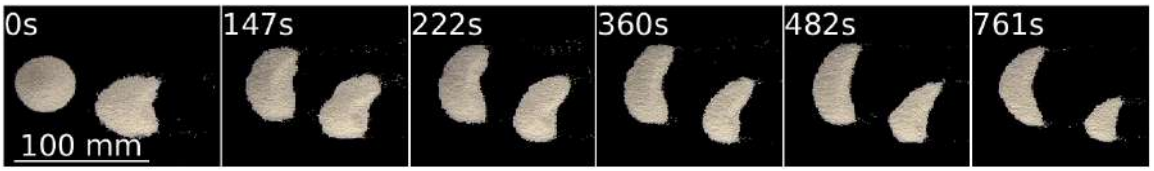

(a)

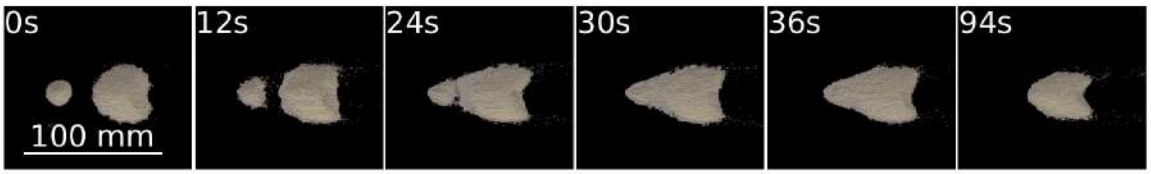

(b)

Figure S13. Snapshots of barchan interactions for off-centered and aligned dunes consisting of zirconium beads with 0.40 mm $\leq d \leq$ 0.60. In the snapshots, the water flow is from left to right, and the corresponding times are shown in each frame. (a) Chasing (off-centered, test 47 of Fig. S24); (b) merging (aligned, test 27 of Fig. S23).

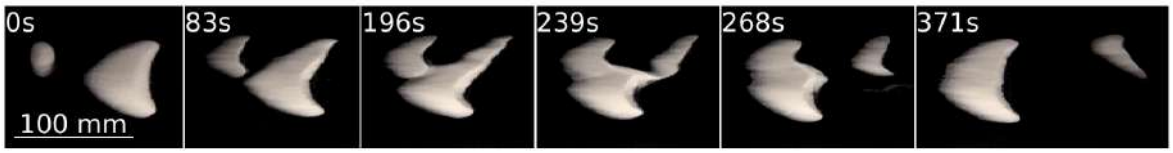

(a)

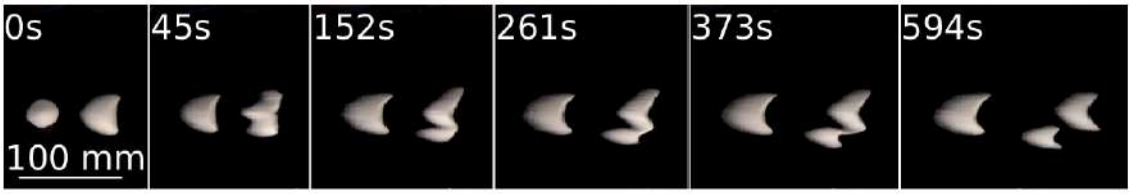

(b)

Figure S14. Snapshots of barchan interactions for off-centered and aligned dunes consisting of angular glass beads with 0.21 mm $\leq d \leq$ 0.30 mm. In the snapshots, the water flow is from left to right, and the corresponding times are shown in each frame. (a) Exchange (off-centered, test 18 of Fig. S24); (b) fragmentation-chasing (aligned, test 63 of Fig. S23).

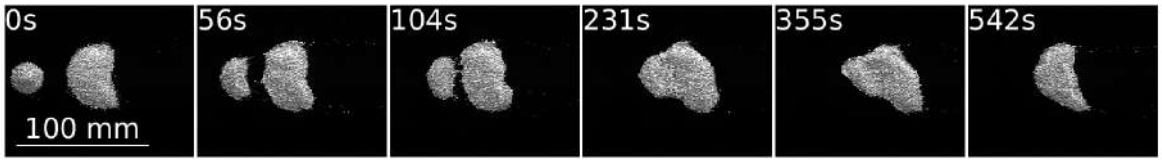

(a)

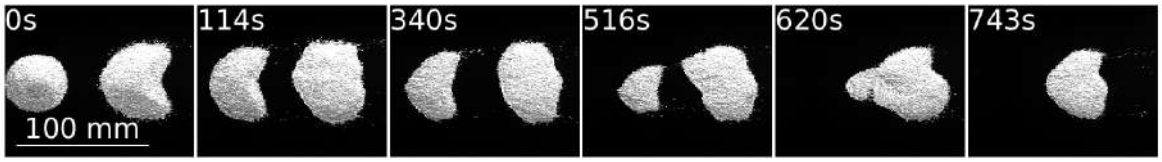

(b)

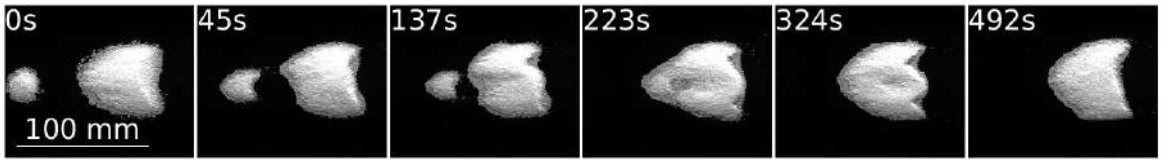

(c)

Figure S15. Snapshots of merging patterns for aligned dunes. In the snapshots, the water flow is from left to right, and the corresponding times are shown in each frame. (a) and (b) Zirconium beads with 0.40 mm $\leq d \leq$ 0.60 (tests 8 and 41 of Fig. S23, respectively); (c) glass beads with 0.40 mm $\leq d \leq$ 0.60 mm (test 20 of Fig. S23).

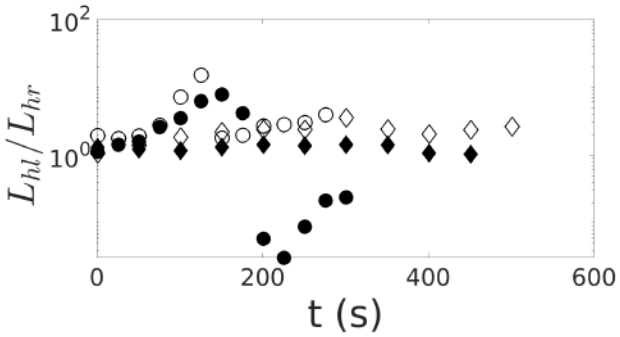

Figure S16. Ratio between the lengths of the left and right horns, L_{hl}/L_{hr}, of the downstream dune along time. Diamonds and circles correspond to the merging and exchange patterns, respectively. Open symbols correspond to the aligned and solid symbols to off-centered cases (they correspond to tests 65 and 36 of Fig. S23, and 38 and 41 of Fig. S24).

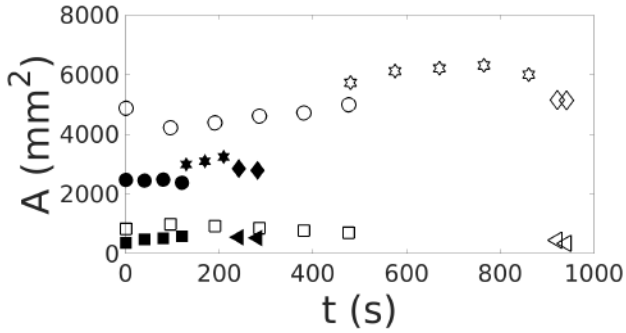

Figure S17. Area variation along time for the exchange pattern. Squares and circles correspond to the initial upstream (impact) and downstream (target) barchans, respectively, stars to the merged bedform, and diamonds and triangles to the merged bedform and new (expelled) barchan, respectively. Open symbols correspond to the aligned and solid symbols to off-centered cases (tests 38 of Fig. S23 and 18 of Fig. S24).

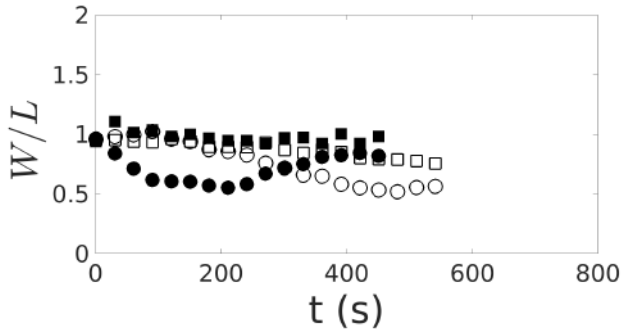

Figure S18. Evolution of W/L along time for the chasing pattern. Squares and circles correspond to the initial upstream (impact) and downstream (target) barchans, respectively. Open symbols correspond to the aligned and solid symbols to off-centered cases (tests 61 of Fig. S23 and 43 of Fig. S24).

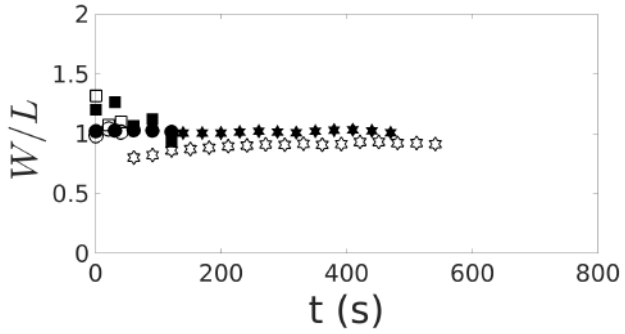

Figure S19. Evolution of W/L along time for the merging pattern. Squares and circles correspond to the initial upstream (impact) and downstream (target) barchans, respectively, and stars to the merged bedform. Open symbols correspond to the aligned and solid symbols to off-centered cases (tests 65 of Fig. S23 and 38 of Fig. S24).

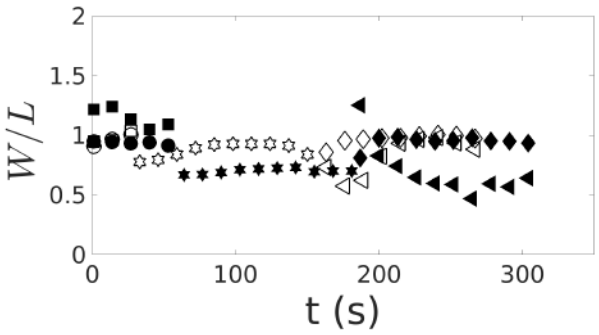

Figure S20. Evolution of W/L along time for the exchange pattern. Squares and circles correspond to the initial upstream (impact) and downstream (target) barchans, respectively, stars to the merged bedform, and diamonds and triangles to the merged bedform and new (expelled) barchan, respectively. Open symbols correspond to the aligned and solid symbols to off-centered cases (tests 36 of Fig. S23 and 41 of Fig. S24).

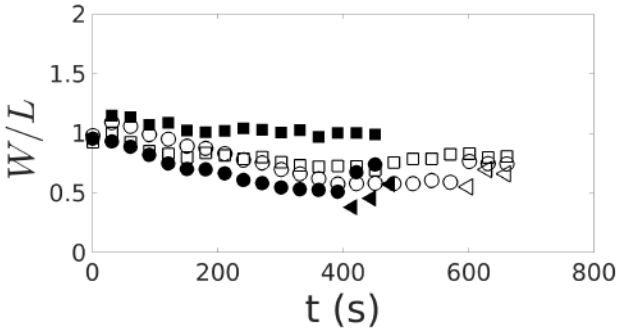

Figure S21. Evolution of W/L along time for the fragmentation-chasing pattern. Squares and circles correspond to the initial upstream (impact) and downstream (target) barchans, respectively, and triangles to the new (expelled) barchan, respectively. Open symbols correspond to the aligned and solid symbols to off-centered cases (tests 5 of Fig. S23 and 31 of Fig. S24).

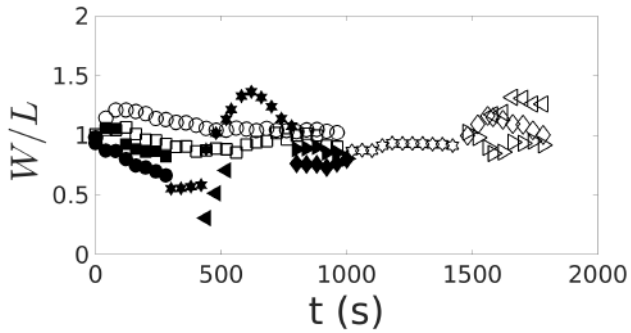

Figure S22. Evolution of W/L along time for the fragmentation-exchange pattern. Squares and circles correspond to the initial upstream (impact) and downstream (target) barchans, respectively, stars to the merged bedform, diamonds and right triangles to upstream and downstream bedforms generated by the split of the merged barchan, respectively, and left triangles to the new (expelled) barchan ("baby" barchan). Open symbols correspond to the aligned and solid symbols to off-centered cases (tests 22 of Fig. S23 and 5 of Fig. S24).

Aligned position															
#	η	σ	$\Delta x_b/D$	$\Delta x_c/D$	m_i	m_t	N_i	N_t	ξ_N	ρ_s	d	u_*	Re_*	θ	Pattern
-	(mm)	-	-	-	(g)	(g)	-	-	-	(kg/m^3)	(mm)	(m/s)	-	-	-
1	-3	-0.07	0.97	2.83	2.0	8.0	12223	48892	0.60	2500	0.50	0.0141	7	0.027	Exchange
2	-2	-0.04	0.82	2.56	2.0	8.0	12223	48892	0.60	2500	0.50	0.0150	8	0.031	Exchange
3	-2	-0.04	0.68	2.48	2.0	8.0	12223	48892	0.60	2500	0.50	0.0159	8	0.034	Exchange
4	-5	-0.12	0.66	2.34	2.0	8.0	190986	763944	0.60	2500	0.20	0.0141	3	0.068	Frag-Chasing
5	2	0.05	0.73	2.43	2.0	8.0	190986	763944	0.60	2500	0.20	0.0159	3	0.086	Frag-Chasing
6	0	-0.01	1.01	2.66	2.0	8.0	91069	364277	0.60	2500	0.26	0.0141	4	0.053	Frag-Chasing
7	-2	-0.05	0.80	2.46	2.0	8.0	91069	364277	0.60	2500	0.26	0.0168	4	0.075	Frag-Chasing
8	-1	-0.03	0.77	2.14	2.0	8.0	7453	29812	0.60	4100	0.50	0.0168	8	0.019	Merging
9	-3	-0.07	0.79	2.21	2.0	8.0	7453	29812	0.60	4100	0.50	0.0185	9	0.022	Merging
10	0	0.00	1.05	2.50	2.0	8.0	7453	29812	0.60	4100	0.50	0.0202	10	0.026	Merging
11	2	0.03	0.70	2.14	4.0	8.0	24446	48892	0.33	2500	0.50	0.0141	7	0.027	Frag-Chasing
12	2	0.05	0.60	2.07	4.0	8.0	24446	48892	0.33	2500	0.50	0.0159	8	0.034	Frag-Exchange
13	1	0.03	0.80	2.01	4.0	8.0	381972	763944	0.33	2500	0.20	0.0141	3	0.068	Frag-Chasing
14	-1	-0.01	0.74	1.93	4.0	8.0	381972	763944	0.33	2500	0.20	0.0159	3	0.086	Frag-Chasing
15	1	0.02	0.67	2.15	4.0	8.0	182138	364277	0.33	2500	0.26	0.0141	4	0.053	Frag-Chasing
16	2	0.05	0.74	2.12	4.0	8.0	182138	364277	0.33	2500	0.26	0.0159	4	0.067	Frag-Chasing
17	4	0.09	0.75	1.99	4.0	8.0	14906	29812	0.33	4100	0.50	0.0168	8	0.019	Merging
18	1	0.03	0.50	1.68	4.0	8.0	14906	29812	0.33	4100	0.50	0.0185	9	0.022	Merging
19	-3	-0.05	0.52	1.72	8.0	16.0	29812	59624	0.33	4100	0.50	0.0185	9	0.022	Merging
20	-5	-0.11	1.13	3.11	1.0	8.0	6112	48892	0.78	2500	0.50	0.0141	7	0.027	Merging
21	-3	-0.06	1.18	3.26	1.0	8.0	6112	48892	0.78	2500	0.50	0.0159	8	0.034	Merging
22	0	0.00	0.76	2.75	1.0	8.0	95493	763944	0.78	2500	0.20	0.0141	3	0.068	Frag-Exchange
23	-3	-0.08	1.02	3.03	1.0	8.0	95493	763944	0.78	2500	0.20	0.0159	3	0.086	Frag-Chasing
24	-3	-0.08	0.83	2.76	1.0	8.0	95493	763944	0.78	2500	0.20	0.0168	3	0.096	Frag-Exchange
25	-5	-0.14	0.84	2.66	1.0	8.0	45535	364277	0.78	2500	0.26	0.0141	4	0.053	Frag-Exchange
26	1	0.03	1.14	2.58	1.0	8.0	3727	29812	0.78	4100	0.50	0.0185	9	0.022	Merging
27	1	0.04	0.77	2.45	1.0	8.0	3727	29812	0.78	4100	0.50	0.0202	10	0.027	Merging
28	0	0.00	0.51	2.02	3.0	8.0	18335	48892	0.45	2500	0.50	0.0141	7	0.027	Merging
29	-3	-0.06	0.47	1.99	3.0	8.0	18335	48892	0.45	2500	0.50	0.0159	8	0.034	Exchange
30	-1	-0.02	1.51	4.67	0.3	14.0	1833	85562	0.96	2500	0.50	0.0141	7	0.027	Merging
31	-4	-0.17	1.44	4.35	0.1	3.0	9549	286479	0.94	2500	0.20	0.0141	3	0.068	Merging
32	-3	-0.11	1.12	3.77	0.1	3.0	9549	286479	0.94	2500	0.20	0.0159	3	0.086	Merging
33	-3	-0.06	1.39	4.24	0.3	14.0	28648	1336902	0.96	2500	0.20	0.0141	3	0.068	Exchange
34	-2	-0.06	1.42	4.15	0.3	8.0	28648	763944	0.93	2500	0.20	0.0141	3	0.068	Exchange
35	-5	-0.15	1.25	3.64	0.3	4.0	28648	381972	0.86	2500	0.20	0.0141	3	0.068	Exchange
36	2	0.04	1.01	4.48	0.3	14.0	28648	1336902	0.96	2500	0.20	0.0159	3	0.086	Exchange
37	0	0.01	1.38	4.09	0.3	14.0	13660	637484	0.96	2500	0.26	0.0141	4	0.053	Exchange
38	-7	-0.13	0.65	2.75	2.0	16.0	12223	97785	0.78	2500	0.50	0.0141	7	0.027	Exchange
39	-4	-0.07	0.53	2.34	3.0	20.0	18335	122231	0.74	2500	0.50	0.0141	7	0.027	Exchange
40	0	0.01	0.71	2.59	3.0	18.0	286479	1718873	0.71	2500	0.20	0.0141	3	0.068	Frag-Exchange
41	-2	-0.03	0.54	1.76	12.0	16.0	44719	59624	0.14	4100	0.50	0.0185	9	0.022	Merging
42	-3	-0.09	0.83	2.79	0.5	6.0	47746	572958	0.85	2500	0.20	0.0159	3	0.086	Frag-Exchange
43	-3	-0.08	1.13	3.51	0.3	6.0	28648	572958	0.90	2500	0.20	0.0159	3	0.086	Exchange
44	-5	-0.15	1.45	3.92	0.3	6.0	13660	273208	0.90	2500	0.26	0.0141	4	0.053	Exchange
45	-4	-0.10	2.18	6.33	0.1	20.0	4553	910692	0.99	2500	0.26	0.0141	4	0.053	Merging
46	-3	-0.10	0.63	1.95	1.5	2.0	68302	91069	0.14	2500	0.26	0.0141	4	0.053	Frag-Chasing
47	-1	-0.03	0.65	1.80	3.0	3.0	136604	136604	0.00	2500	0.26	0.0141	4	0.053	Frag-Chasing
48	-3	-0.09	0.68	2.14	1.5	4.0	68302	182138	0.45	2500	0.26	0.0159	4	0.067	Frag-Chasing
49	-1	-0.01	0.46	1.70	2.0	4.0	12223	24446	0.33	2500	0.50	0.0133	7	0.024	Merging
50	-3	-0.07	0.94	3.11	0.6	8.0	3667	48892	0.86	2500	0.50	0.0141	7	0.027	Merging

Aligned position – Continuation															
#	η	σ	$\Delta x_b/D$	$\Delta x_c/D$	m_i	m_t	N_i	N_t	ξ_N	ρ_s	d	u_*	Re_*	θ	*Pattern*
-	(mm)	-	-	-	(g)	(g)	-	-	-	(kg/m^3)	(mm)	(m/s)	-	-	-
51	0	-0.01	0.92	2.83	0.7	12.0	2609	44719	0.89	4100	0.50	0.0185	9	0.022	Merging
52	-1	-0.04	0.59	1.94	1.5	2.0	143239	190986	0.14	2500	0.20	0.0141	3	0.068	Frag-Chasing
53	0	-0.01	0.50	1.71	3.0	3.0	286479	286479	0.00	2500	0.20	0.0159	3	0.086	Chasing
54	0	0.01	0.22	1.40	9.0	10.0	33539	37266	0.05	4100	0.50	0.0202	10	0.027	Chasing
55	1	0.01	0.45	1.76	10.0	10.0	61115	61115	0.00	2500	0.50	0.0141	7	0.027	Chasing
56	2	0.04	0.38	1.67	9.0	10.0	55004	61115	0.05	2500	0.50	0.0159	8	0.034	Exchange
57	0	-0.01	0.59	1.79	2.7	3.0	257831	286479	0.05	2500	0.20	0.0141	3	0.068	Frag-Chasing
58	0	0.01	0.65	1.90	2.7	3.0	257831	286479	0.05	2500	0.20	0.0159	3	0.086	Chasing
59	2	0.04	0.48	1.71	3.0	3.0	286479	286479	0.00	2500	0.20	0.0141	3	0.068	Frag-Chasing
60	1	0.03	0.58	1.91	2.7	3.0	16501	18335	0.05	2500	0.50	0.0159	8	0.034	Chasing
61	5	0.07	0.52	1.65	10.0	10.0	61115	61115	0.00	2500	0.50	0.0159	8	0.034	Chasing
62	2	0.04	0.54	1.86	6.0	8.0	36669	48892	0.14	2500	0.50	0.0159	8	0.034	Frag-Chasing
63	2	0.04	0.83	2.12	3.0	3.0	136604	136604	0.00	2500	0.26	0.0141	4	0.053	Frag-Chasing
64	1	0.02	0.71	1.96	2.7	3.0	122943	136604	0.05	2500	0.26	0.0141	4	0.053	Frag-Chasing
65	-1	-0.03	0.89	4.71	0.1	20.0	9549	1909860	0.99	2500	0.20	0.0141	3	0.068	Merging
66	2	0.03	1.56	2.66	10.0	10.0	61115	61115	0.00	2500	0.50	0.0159	8	0.034	Chasing
67	3	-0.08	3.59	6.63	0.1	20.0	9549	1909860	0.99	2500	0.20	0.0141	3	0.068	Merging
68	1	-0.02	3.39	5.89	0.3	14.0	28648	1336902	0.96	2500	0.20	0.0159	3	0.086	Exchange
69	3	-0.08	1.91	3.15	2.0	8.0	190986	763944	0.60	2500	0.20	0.0159	3	0.086	Frag-Chasing
70	3	0.07	1.95	3.41	1.0	8.0	95493	763944	0.78	2500	0.20	0.0141	3	0.068	Frag-Exchange

Figure S23. List of the tested conditions in the aligned configuration. η is the offset distance between the centroids, σ is the offset parameter, $\Delta x_b/D$ and $\Delta x_c/D$ are the initial distances between dune borders and centroids, respectively, normalized by the initial diameter of the impact pile, m_i and m_t are the masses of the impacting (upstream) and target (downstream) dunes, respectively, N_i and N_t are the number of grains of the impacting and target dunes, respectively, ξ_N is the dimensionless particle number, ρ_s and d are the density and mean diameter of grains, respectively, u_* is the shear velocity, Re_* is the particle Reynolds number, θ is the Shields number, and *Pattern* corresponds to the collision pattern.

Off-centered position															
#	η	σ	$\Delta x_b/D$	$\Delta x_c/D$	m_i	m_t	N_i	N_t	ξ_N	ρ_s	d	u_*	Re_*	θ	*Pattern*
-	(mm)	-	-	-	(g)	(g)	-	-	-	(kg/m³)	(mm)	(m/s)	-	-	-
1	22	0.49	0.48	2.16	2.0	8.0	12223	48892	0.60	2500	0.50	0.0141	7	0.027	Merging
2	28	0.66	0.57	2.18	2.0	8.0	12223	48892	0.60	2500	0.50	0.0150	8	0.031	Merging
3	25	0.58	0.38	2.03	2.0	8.0	12223	48892	0.60	2500	0.50	0.0159	8	0.034	Merging
4	26	0.59	0.46	2.01	2.0	8.0	190986	763944	0.60	2500	0.20	0.0141	3	0.068	Frag-Exchange
5	17	0.39	0.43	2.15	2.0	8.0	190986	763944	0.60	2500	0.20	0.0159	3	0.086	Frag-Exchange
6	16	0.43	0.40	1.70	2.0	8.0	7453	29812	0.60	4100	0.50	0.0168	8	0.019	Merging
7	17	0.48	0.39	1.86	2.0	8.0	7453	29812	0.60	4100	0.50	0.0202	10	0.027	Merging
8	25	0.52	0.42	1.72	4.0	8.0	24446	48892	0.33	2500	0.50	0.0141	7	0.027	Chasing
9	22	0.47	0.60	1.94	4.0	8.0	24446	48892	0.33	2500	0.50	0.0159	8	0.034	Chasing
10	24	0.50	0.66	2.03	4.0	8.0	381972	763944	0.33	2500	0.20	0.0141	3	0.068	Chasing
11	27	0.60	0.30	1.77	4.0	8.0	381972	763944	0.33	2500	0.20	0.0159	3	0.086	Frag-Chasing
12	16	0.40	0.57	1.80	4.0	8.0	14906	29812	0.33	4100	0.50	0.0168	8	0.019	Chasing
13	15	0.38	0.40	1.68	4.0	8.0	14906	29812	0.33	4100	0.50	0.0202	10	0.027	Merging
14	24	0.57	0.79	2.69	1.0	8.0	6112	48892	0.78	2500	0.50	0.0141	7	0.027	Merging
15	22	0.51	0.73	2.68	1.0	8.0	6112	48892	0.78	2500	0.50	0.0159	8	0.034	Merging
16	21	0.52	0.41	2.37	1.0	8.0	95493	763944	0.78	2500	0.20	0.0141	3	0.068	Exchange
17	21	0.53	0.52	2.49	1.0	8.0	95493	763944	0.78	2500	0.20	0.0159	3	0.086	Exchange
18	18	0.40	1.09	2.67	1.0	8.0	45535	364277	0.78	2500	0.26	0.0159	4	0.067	Exchange
19	14	0.43	0.47	2.19	1.0	8.0	3727	29812	0.78	4100	0.50	0.0168	8	0.019	Merging
20	16	0.48	0.53	2.30	1.0	8.0	3727	29812	0.78	4100	0.50	0.0202	10	0.027	Merging
21	26	0.57	0.61	2.08	3.0	8.0	18336	48892	0.45	2500	0.50	0.0141	7	0.027	Chasing
22	23	0.49	0.63	2.02	3.0	8.0	18336	48892	0.45	2500	0.50	0.0159	8	0.034	Merging
23	19	0.40	0.82	2.28	3.0	8.0	136604	364277	0.45	2500	0.26	0.0141	4	0.053	Frag-Exchange
24	19	0.41	0.63	2.02	3.0	8.0	286479	763944	0.45	2500	0.20	0.0159	3	0.086	Frag-Chasing
25	19	0.43	0.78	2.26	3.0	8.0	286479	763944	0.45	2500	0.20	0.0176	4	0.106	Frag-Chasing
26	15	0.38	0.45	1.69	3.0	8.0	11181	29812	0.45	4100	0.50	0.0168	8	0.019	Merging
27	16	0.41	0.33	1.52	3.0	8.0	11181	29812	0.45	4100	0.50	0.0202	10	0.027	Merging
28	22	0.43	0.58	1.81	6.0	8.0	36669	48892	0.14	2500	0.50	0.0141	7	0.027	Chasing
29	17	0.32	0.62	1.89	6.0	8.0	36669	48892	0.14	2500	0.50	0.0159	8	0.034	Chasing
30	20	0.39	0.81	2.06	6.0	8.0	572958	763944	0.14	2500	0.20	0.0141	3	0.068	Chasing
31	21	0.41	0.53	1.94	6.0	8.0	572958	763944	0.14	2500	0.20	0.0159	3	0.086	Frag-Chasing
32	16	0.37	0.40	1.57	6.0	8.0	22359	29812	0.14	4100	0.50	0.0168	8	0.019	Chasing
33	15	0.37	0.39	1.61	6.0	8.0	22359	29812	0.14	4100	0.50	0.0202	10	0.027	Chasing
34	32	0.72	0.91	3.70	0.3	14.0	1833	85562	0.96	2500	0.50	0.0141	7	0.027	Merging
35	20	0.46	1.45	4.27	0.3	14.0	1833	85562	0.96	2500	0.50	0.0159	8	0.034	Merging
36	22	0.48	1.01	3.22	0.3	14.0	28648	1336902	0.96	2500	0.20	0.0141	3	0.068	Exchange
37	24	0.54	0.65	3.01	0.3	14.0	28648	1336902	0.96	2500	0.20	0.0159	3	0.086	Exchange
38	20	0.43	1.13	5.87	0.1	20.0	9549	1909859	0.99	2500	0.20	0.0141	3	0.068	Merging
39	17	0.38	1.27	5.45	0.1	20.0	9549	1909859	0.99	2500	0.20	0.0159	3	0.086	Exchange
40	15	0.42	0.89	3.28	0.5	6.0	47746	572958	0.85	2500	0.20	0.0141	3	0.068	Exchange
41	12	0.35	0.79	2.95	0.5	6.0	47746	572958	0.85	2500	0.20	0.0159	3	0.086	Exchange
42	19	0.49	0.90	2.16	3.0	3.0	286479	286479	0.00	2500	0.20	0.0141	3	0.068	Chasing
43	15	0.41	0.52	1.84	3.0	3.0	286479	286479	0.00	2500	0.20	0.0159	3	0.086	Chasing
44	14	0.34	0.68	1.80	3.0	3.0	136604	136604	0.00	2500	0.26	0.0141	4	0.053	Frag-Chasing
45	20	0.34	0.52	1.76	10.0	10.0	61115	61115	0.00	2500	0.50	0.0141	7	0.027	Chasing
46	20	0.33	0.59	1.83	10.0	10.0	61115	61115	0.00	2500	0.50	0.0159	8	0.034	Chasing
47	17	0.38	0.35	1.51	8.0	8.0	29812	29812	0.00	4100	0.50	0.0168	8	0.019	Chasing
48	16	0.37	0.43	1.60	8.0	8.0	29812	29812	0.00	4100	0.50	0.0202	10	0.027	Chasing
49	16	0.49	1.42	2.33	3.0	3.0	286479	286479	0.00	2500	0.20	0.0159	3	0.086	Chasing
50	16	0.41	2.78	6.22	0.1	20.0	9549	1909859	0.99	2500	0.20	0.0141	3	0.068	Merging
51	14	0.42	2.03	3.58	0.5	6.0	47746	572958	0.85	2500	0.20	0.0159	3	0.086	Exchange
52	27	0.63	1.22	2.29	6.0	8.0	572958	763944	0.14	2500	0.20	0.0159	3	0.086	Frag-Chasing
53	13	0.35	1.40	2.70	2.0	8.0	190986	763944	0.60	2500	0.20	0.0159	3	0.086	Frag-Exchange

Figure S24. List of the tested conditions in the off-centered configuration. η is the offset distance between the centroids, σ is the offset parameter, $\Delta x_b/D$ and $\Delta x_c/D$ are the initial distances between dune borders and centroids, respectively, normalized by the initial diameter of the impact pile, m_i and m_t are the masses of the impacting (upstream) and target (downstream) dunes, respectively, N_i and N_t are the number of grains of the impacting and target dunes, respectively, ξ_N is the dimensionless particle number, ρ_s and d are the density and mean diameter of grains, respectively, u_* is the shear velocity, Re_* is the particle Reynolds number, θ is the Shields number, and *Pattern* corresponds to the collision pattern.

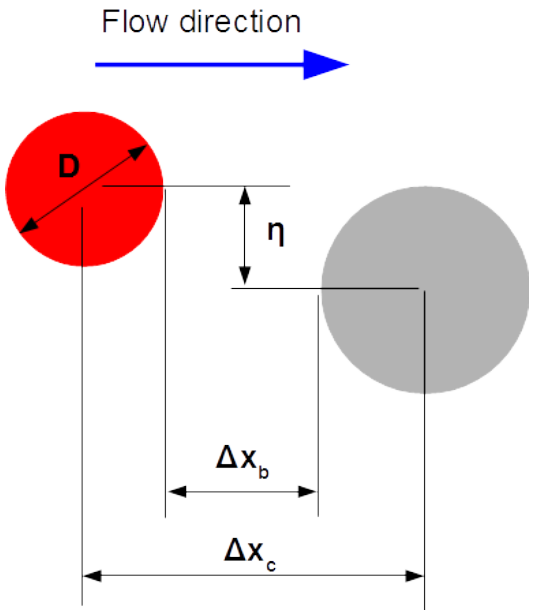

Figure S25. Offset distance, η, and initial distances between dune borders and centroids in the longitudinal direction, Δx_b and Δx_c, respectively, as listed in Figs. S23 and S24.

Table S1. Cross-sectional mean velocity U, shear velocity u_*, experimentally determined Darcy friction factor f, and Darcy friction factor from the Blasius correlation f_{bla}, for each Reynolds numbers Re and Re_{dh}.

Re	Re_{dh}	U	u_*	f	f_{bla}
$\cdots$	$\cdots$	m/s	m/s	$\cdots$	$\cdots$
2.43×10^4	1.65×10^4	0.243	0.0147	0.0293	0.0279
2.94×10^4	1.99×10^4	0.294	0.0173	0.0277	0.0266
3.64×10^4	2.47×10^4	0.364	0.0210	0.0266	0.0252

Table S2. Figure number, test number, area of the impact barchan A_i, area of the expelled barchan A_e, and ratio between areas of expelled and impact barchans A_e/A_i, for the exchange pattern. A_i and A_e correspond to averages over time of areas just before collision (for the impact barchan) and after being expelled (for the ejected barchan), respectively.

Figure # ...	Test # ...	A_i mm^2	A_e mm^2	A_e/A_i ...
S23	35	427	296	0.69
S23	36	337	559	1.66
S23	38	706	540	0.76
S23	39	1179	1852	1.57
S23	43	381	275	0.72
S23	44	401	638	1.59
S23	68	333	180	0.54
S24	17	401	638	1.59
S24	18	594	545	0.92
S24	36	378	659	1.74
S24	37	356	909	2.56
S24	39	136	81	0.59
S24	40	568	825	1.45
S24	41	466	981	2.10
S24	51	655	997	1.52